Synergistic Integration and Pharmacomechanical Function of Enzyme-Magnetite Nanoparticle Swarms for Low-Dose Fast Thrombolysis

WILEY-VCH

Synergistic Integration and Pharmacomechanical Function of Enzyme-magnetite Nanoparticle Swarms for Low-dose Fast Thrombolysis

Xiuzhen Tang,[#] Laliphat Manamanchaiyaporn,[#] Qi Zhou,[#] Chenyang Huang, Lihuang Li, Ziqiao Li, Longchen Wang, Jienan Wang, Lei Ren, Tiantian Xu, Xiaohui Yan, * Yuanyi Zheng**

X. Tang, L. Wang, J Wang, Y. Zheng
Department of Ultrasound in Medicine, Shanghai Jiao Tong University Affiliated Sixth People's Hospital, Shanghai Institute of Ultrasound in Medicine
200233, P. R. China
E-mail: zhengyuanyi@sjtu.edu.cn

L. Li, Z. Li, X. Yan
State Key Laboratory of Molecular Vaccinology and Molecular Diagnostics & Center for Molecular Imaging and Translational Medicine, School of Public Health, Xiamen University
361104, P. R. China
E-mail: xhyan@xmu.edu.cn

C. Huang, T. Xu
Guangdong Provincial Key Laboratory of Robotics and Intelligent System, Shenzhen Institutes of Advanced Technology, Chinese Academy of Sciences
518055, P. R. China
E-mail: tt.xu@siat.ac.cn

X. Tang, L. Manamanchaiyaporn
Center of Excellence in Creative Engineering Design and Development & Department of Mechanical Engineering, Faculty of Engineering, Thammasat University
12121, Thailand

Q. Zhou
School of Engineering, Institute for Multiscale Thermofluids, University of Edinburgh
EH9 3FB, Edinburgh, UK

L. Huang, L. Ren
Department of Biomaterials, College of Materials, Xiamen University
361005, P. R. China

Keywords: magnetite nanoparticles, swarm control, magnetic field, enzyme, thrombolysis

Magnetic micro-/nanoparticles have been extensively explored over the past decade as active diagnostic/therapeutic agents for minimally invasive medicine. However, sufficient function integration on these miniaturized bodies towards practical applications remains challenging. This work proposes a synergistic strategy via integrating particle functionalization and bioinspired swarming, demonstrated by recombinant tissue plasminogen activator modified magnetite nanoparticles (rtPA-Fe_3O_4 NPs) for fast thrombolysis *in vivo* with low drug dosage. The synthesized rtPA-Fe_3O_4 NPs exhibit superior magnetic performance, high biocompatibility and thrombolytic enzyme activity. Benefiting from a customized magnetic operation system designed for animal experiments and preclinical development, these agglomeration-free NPs can assemble into micro-/milli-scale swarms capable of robust maneuver and reconfigurable transformation for on-demand tasks in complex biofluids. Specifically, the spinning mode of the swarm exerts focused fluid shear stresses while rubbing on the thrombus surface, constituting a mechanical force for clot breakdown. The synergy of the NPs' inherent enzymatic effect and swarming-triggered fluid forces enables amplified efficacy of thrombolysis in an in vivo occlusion model of rabbit carotid artery, with lower drug concentration than clinical dosage. Furthermore, swarming-enhanced ultrasound signals aid in imaging-guided treatment. Therefore, the pharmacomechanical NP swarms herein represent an injectable thrombolytic tool joining advantages of intravenous drug therapy and robotic intervention.

1. Introduction

Synthetic micro-/nanoparticles have been extensively explored for applications in realms of innovative biomedicine, green energy, efficient catalysis, among others[1, 2]. Their intrinsic small dimensions endow them with fast dispersion, high surface activity and various other advantageous properties inaccessible for their bulk counterpart, but at the same time, bring challenges to effective integration of sufficient functions on them for designated applications. Functionalization of these micro-/nanoparticles has been widely exploited, for which common engineering strategies include matrix selection, architecture design and surface modification[1, 2-4]. One barrier for synthesizing multifunctional micro-/nanoparticles is that specific materials or protocols (sometimes not available at all) are usually required for different functionalization needs, and new synthesis strategies remain to be innovated for integrating the require functions through cost-effective mass production while maintaining low environmental impact. Apart from functionalization, mimicking natural swarming evolved in living systems/organisms, such

as ant colonies transporting cargo much larger than their body weight and grid-like herring school capturing alert copepods, offers an alternative pathway for advanced functions through collective behavior. Biological swarming is usually sophisticated yet orderly patterned and exhibits intriguing synergistic effects that can enable complex tasks unattainable by an individual entity or the entities of arbitrary organization[5].

To date, many attempts have been made with active particles comprising compositions capable of responding to chemical signals or physical stimuli exerted by external fields, *e.g.,* light, ultrasound, electric field and magnetic field[6, 7, 8-11]. In the field of biomedicine, magnetic particles attract wide attention over recent years. First of all, the application of magnetic fields as the stimulus (or power source) features continuous power transmission, precise control, high penetration depth and minimal invasiveness[3, 4, 12]. Furthermore, equipped with proper magnetic fields, the magnetic particles can form patterned swarms as chains, ribbons and vortices through magnetization-triggered dipole-dipole interactions and motion-induced hydrodynamic interactions[7, 8-11]. The swarms show robust maneuverability and possess key functions of natural swarming, such as coordinated locomotion, collaborative manipulation and on-demand transformation, therefore suggesting an ability of navigating hard-to-reach regions to perform complex assignments. Additionally, benefiting from swarming, the magnetization strength, imaging signal, cargo-loading capacity and other quantity-dependent properties of the magnetic particles are substantially enhanced on site[7, 8-11, 13, 14]. The threefold advantages mentioned above make magnetically-assembled swarms promising for various biomedical applications, *e.g.,* biopsy, targeted delivery and minimally-invasive surgery. For instance, significant progress has been made in targeted delivery using magnetite (Fe_3O_4) particles, which are potential diagnostic/therapeutic agents featuring high biosafety, easy functionalization and superior actuation performance[2-4, 9, 11, 13, 14]. Previous studies have demonstrated swarming of Fe_3O_4 particles in biological fluids[13], transport of thrombolytic drug by swarming-induced microfluidic effects[14], and possible endovascular delivery under ultrasound monitoring[9].

This work aims to exploit the potential of magnetic swarms comprising pharmacologically functionalized Fe_3O_4 nanoparticles for fast treatment of thrombus *in vivo*, which is a global health issue that costs millions of lives each year[15]. Thrombosis (the formation of thrombus) can occlude blood vessels and disrupt normal blood circulation, causing insufficient supply of oxygen as well as nutrients and eventually leading to tissue damage and organ failure. It may also trigger other fatal medical conditions, such as cerebral stroke, coronary heart disease and pulmonary embolism. The acute cut-off of blood supply is the primary reason for the high disability and mortality rates arising from thrombosis[16, 17].

Therefore, timely restoration of the blood flow at the early stage can prevent tissue ischemia and improve the prognosis of patients. To realize this in clinic, intravenous thrombolytic drug therapy and surgical intervention are feasible approaches[16, 18]. Commonly used drugs include urokinase plasminogen activator (uPA), tissue plasminogen activator (tPA), recombinant tPA (rtPA), vitamin K antagonists, streptokinase (SK) and heparin[16, 19]. Despite progress, rapid elimination of these drug agents from the human body (whose circulation half-life are usually less than 5 min) poses a critical challenge for therapeutic efficacy *in vivo*. This is because more administration cycles and higher dosage are needed for thrombus therapy, which indicates increased risks of bleeding complications. On the other hand, surgical intervention such as catheter-directed thrombolysis can potentially overcome these issues[20]. However, such treatment is usually associated with high cost, surgical incision and inadequate capability of reaching secondary vessels. In view of the above, more robust therapeutics is required for clinical thrombolysis.

Prior works on magnetic micro-/nanomotors for thrombus therapy have focused on their assistive roles in enhancing drug diffusion[21, 22] or introducing interfacial flows[14]. Such efforts made progress in accelerating the thrombolytic efficacy, but the concentration of thrombolytic drug needed was still too high compared to clinical dosage, hindering potential applications *in vivo*. Therefore, further integration of the drug agents and the assisting motors is required. In the present study, we achieve this by synthesizing a recombinant tissue plasminogen activator (rtPA, an enzyme ingredient of clinical thrombolytic drugs) modified Fe_3O_4 nanoparticles (rtPA-Fe_3O_4 NPs), and investigate their functionalization/swarming synergy envisioned for fast thrombolysis *in vivo* (**Figure 1**). The synthetic rtPA-Fe_3O_4 NPs integrate multiple desired attributes of nanomedicine from the Fe_3O_4 matrix and rtPA coating, including minimal hemolysis, superparamagnetic property, high magnetization strength, thrombolytic enzyme capacity and low cellular/systemic toxicity. The generation and control of rtPA-Fe_3O_4 swarms relies on rotating/gradient magnetic fields by a maneuverable rotating permanent magnet (MRPM) system. The MRPM system allows the obtained swarms to perform spinning motion, on-demand transformation and three-dimensional (3-D) propulsion in complex microenvironments such as vascular networks. Of special interest is the spinning motion of the swarm, which can enhance the fluid shear stress acting on thrombi in situ to accelerate their lysis. Combined with enzymatic capacity of individual rtPA-Fe_3O_4 entities, the swarming-endowed mechanical forces give rise to a synergistic effect of pharmacomechanical thrombolysis, which substantially enhances the efficiency of thrombus or blood-clot removal. Furthermore, owing to enhanced imaging signals, the rtPA-Fe_3O_4

swarm can be reliably tracked in real-time *via* ultrasound imaging. Our animal trial in a rabbit's carotid artery occlusion model demonstrates *in vivo* efficacy of the proposed pharmacomechanical thrombolysis, where the results indicate high translational prospects of our functionalization/swarming synergy-based therapeutics as a proof-of-concept for potential clinical applications. Taken together, our work herein represents an integrated platform featuring an injectable thrombolytic agent through combined intravenous drug therapy and robotic intervention.

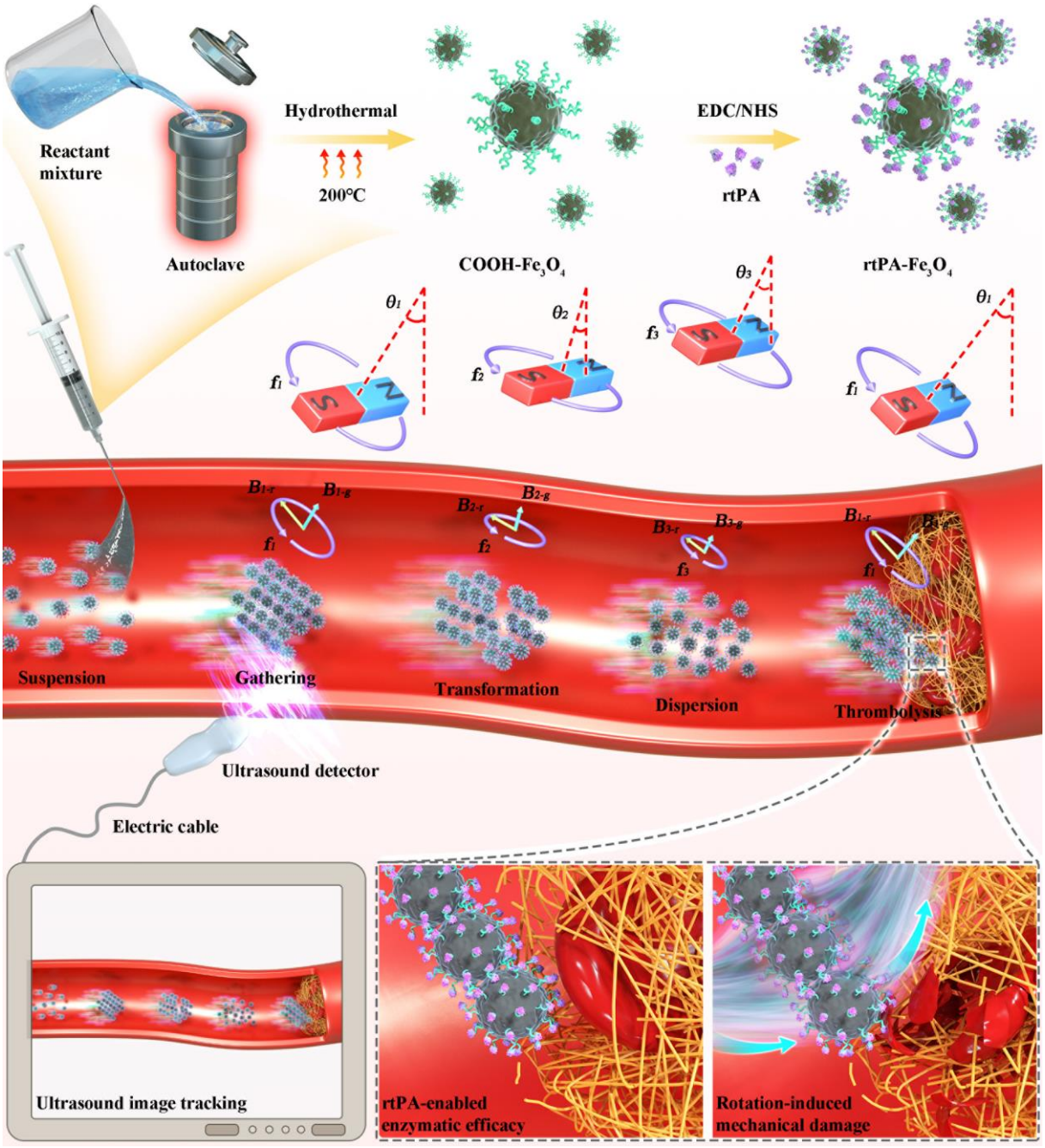

Figure 1. Workflow of pharmacomechanical thrombolysis *in vivo* guided by real-time ultrasound imaging. (**a**) Synthesis of rtPA-Fe_3O_4 nanoparticles (NPs) through a two-step process including hydrothermal and EDC/NHS treatment. The EDC/NHS treatment uses N-

(3-Dimethylaminopropyl)-N'-ethylcarbodiimide hydrochloride (EDC)/N-Hydroxysuccinimide (NHS) chemistry. (**b**) Magnetic control of rtPA-Fe_3O_4 NP swarm to navigate an occluded blood vessel and perform efficient thrombolytic microsurgery using a customized maneuverable rotating permanent magnet (MRPM) system. The symbols θ, f and B represent the pitch angle, the rotation frequency and the magnetic field strength, respectively. The lowercase letter r and g stand for rotating and gradient magnetic fields, respectively. (**c**) Synergistic thrombolysis combining enzymatic activity and swarming-induced mechanical damage as a proof-of-concept for preclinical developments, equipped with ultrasound imaging for real-time tracking and image-guided therapy

2. RESULTS

2.1. Synthesis of rtPA-Fe_3O_4 NPs

As **Figure 1** shows, the synthesis is a two-step process including the addition of a carboxyl group (COOH-Fe_3O_4) and subsequent grafting of rtPA on the surface of Fe_3O_4 NPs. We follow a reported one-pot hydrothermal method[2, 23] for the first step, harvesting a well-dispersed suspension (**Figure S1a, section S1**) consisting of spherical porous COOH-Fe_3O_4 aggregated by small building blocks (~35 nm in diameter, **Figure 2a and b**). Statistical analysis based on the electron micrographs of randomly-selected 50 NPs reports an average diameter for the COOH-Fe_3O_4 NPs of about 440 nm. Subsequent rtPA grafting as the second step employs the N-(3-Dimethylaminopropyl)-N'-ethylcarbodiimide hydrochloride (EDC)/N-Hydroxysuccinimide (NHS) chemistry[24]. In this treatment, the carboxyl on the NPs is activated and covalently bonded with the amino of rtPA. The whole synthesis process features rapid reaction, high efficiency, and more importantly, low/negligible impact on the rtPA's enzyme activity[24]. After the EDC/NHS treatment, transmission electron microscopy (TEM) imaging of the treated NPs demonstrates a layer of low-contrast substance added to the NP periphery (**Figure 2c**, labeled by black arrows). Statistical analysis of the EDC/NHS-treated NP suggests an increase of the average diameter to around 452 nm compared to the COOH-Fe_3O_4 only NP. Further elemental mapping of these NPs identifies the presence of N, P and S elements, which are presumably attributed to the immobilized rtPA (**Figure 2d** and **Figure S1b, Table S1**, section S1). All the evidence above indicates the successful grafting of rtPA onto the COOH-Fe_3O_4 NP, confirmed by additional quantification of the hydrated particle size, zeta potential and surface functional group (**Figure 2e** and **f**). As shown in **Figure 2f,** the C-N and C-H band stretching mode at 1527 and 2922 cm^{-1} from rtPA molecules were only observed in the spectrum of rtPA-Fe_3O_4 but not in that of pristine COOH-Fe_3O_4 sample, indicating the presence

of rtPA in the rtPA-Fe_3O_4 sample. The grafted rtPA is found to have a roughly uniform distribution on the NP surface as the elemental mapping suggests in **Figure 2d**. The eventual grafting ratio of rtPA was determined as 13.25%, with the aid of a human rtPA ELISA kit which measured the residual amount of rtPA in the supernatant solution resulting from grafting process (**Figure S2**, **section S1**). For more information about the drug loading process and grafting ratio calculation, refer to the "Materials and Methods" section). Following X-ray diffraction (XRD) analysis clarifies retention of the Fe_3O_4 phase (PDF reference code 75-1610 for the XRD pattern) in the modified NPs of rtPA-Fe_3O_4 composition (**Figure 2g**), which possess a saturation magnetization (M_s) of 71.00 emu/g (**Figure 2h**) and thus guarantee robust response to externally applied magnetic fields. On the other hand, the remnant magnetization (M_r) is only 3.85 emu/g, suggesting the synthesized rtPA-Fe_3O_4 NPs as superparamagnetic and therefore free-of fatal agglomerates if employed for applications *in vivo*[2-4, 8, 25]. Last but not least, the rtPA-Fe_3O_4 NPs satisfactorily preserve the thrombolytic enzyme activity of the immobilized rtPA (**Figure 2i** and **Figure S3**, **section S1**), which is found positively correlated with the sample concentration but negatively correlated with reaction or storage time.

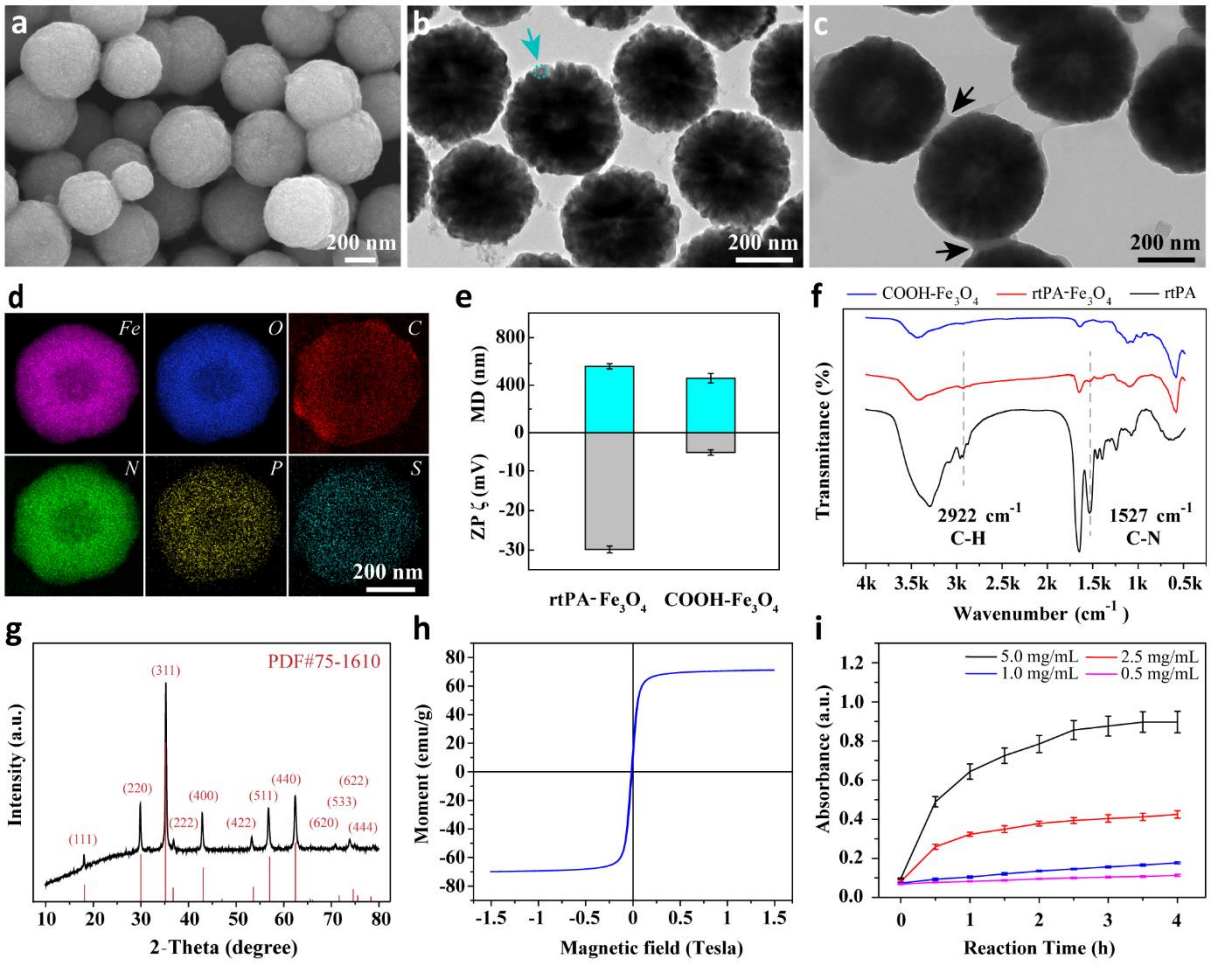

Figure 2. Characterization of rtPA-Fe_3O_4 NPs, COOH-Fe_3O_4 NPs, and free rtPA. (**a** and **b**) SEM and TEM images of the fabricated COOH-Fe_3O_4 NPs, respectively. The light-blue arrow indicates small building blocks (~35 nm in diameter) on the COOH-Fe_3O_4 NP. (**c**) TEM image of the fabricated rtPA-Fe_3O_4 NPs. The black arrows indicate low-contrast substances absent on the surface of COOH-Fe_3O_4 NPs. (**d**) Element mapping of an individual rtPA-Fe_3O_4 NP. The detected signals are distributed throughout the whole NP. (**e**) Hydrated diameter and zeta potential ζ of the COOH-Fe_3O_4 and rtPA-Fe_3O_4 NPs (n = 3). (**f**) Fourier Transform infrared spectroscopy (FTIR) spectra of COOH-Fe_3O_4 NPs, rtPA-Fe_3O_4 MPs, and pure rtPA. The insets show magnification of two peaks on the rtPA-Fe_3O_4 curve. (**g** and **h**) XRD pattern and hysteresis loop for rtPA-Fe_3O_4. (**i**) Time-absorbance plot of S-2288 activity assays indicating enzyme activity of the rtPA immobilized on Fe_3O_4 NPs (n = 3), for which higher absorbance in less time indicates stronger activity, *vice versa*.

2.2. MRPM (maneuverable rotating permanent magnet) manipulator

Magnetic instruments commonly reported for manipulating magnetic particle swarms are electromagnetic coils, *e.g.,* tri-axial Helmholtz coils and iron-cored solenoid coils[7, 8, 13, 14]. With these instruments, the modes and parameters of the applied magnetic field can be accurately adjusted as needed. However, limitations such as insufficient working space, low magnetic-field strength and high heat production hinder the application of the electromagnetic-coil setups towards *in vivo* trials, which are the focus of the present study. We therefore turn to permanent magnet manipulators[3, 4, 9, 26]. Albeit with fewer magnetic-field modes and lower control precision, the permanent magnet manipulators are more flexible in operation space and can potentially overcome the deficiencies of electromagnetic coils for practical animal experiments. To this end, we propose an operating system of maneuverable rotating permanent magnet (MRPM). As depicted in **Figure 3a**, the construction of MRPM is straightforward *via* mounting a permanent magnet onto the end effector of a robotic arm. The arm provides 6 degrees of freedom (DOF), three rotation axes and three orthogonal translation axes (X-axis, Y-axis and Z-axis), allowing both angular and translation control. Variable parameters of the angular control include the rotation angle φ, the yaw angle ϕ and the pitch angle θ (for definition of these parameters, see schematics in **Figure 3b**). θ is the most critical control parameter since it determines the magnetic field mode of the MRPM. φ represents the swiping angle of the magnet over a full rotation cycle, while ϕ captures the curvilinear movement of the magnet in designated planes as a function of translation along the X-axis and Z-axis. Other important parameters include the rotation frequency f (or angular velocity ω) of the magnet, and the

separation distance *d* between the magnet and the target sample (**Figure 3b**). *f* (or ω) indicates the rate of change of the magnetic field, which affects the repulsive/attractive forces between Fe_3O_4 NPs during the process of swarm generation (**section S2**). *d*, a parameter associated with the translation along Y-axis, decides the magnetic strength *B* at the location of the tested sample. Plotting the magnetic field strength *B* at $\theta = 30º, 45º, 60º$ against designated *d* values reveals strong negative correlations, where *B* drastically decreases as *d* increases (**Figure 3c**).

Dynamic distributions of the magnetic field generated by MRPM are first analyzed through numerical simulation. As aforementioned, θ and *d* are crucial parameters for the three-dimensional distributions of the magnetic field surrounding the target sample. Given the negative *B*-*d* correlation as well as the workspace needed for subsequent *in vitro/in vivo* experiments, the testing values of *d* are set between 2 cm and 6 cm. Meanwhile, a wide range of θ values (0°, 15°, 30°, 45°, 60°, 75° and 90°) are examined. **Figure 3d-f** present three sets of desired distributions obtained at $\theta = 30°, 45°, 60°$, respectively. The corresponding simulation videos are provided as **Video S1-3** in the Supplementary Materials. In these distributions, the magnetic field vectors are found to periodically alternate between two half-cycles: focusing inwards to the central region (where the magnet is located) and scattering outwards from the center. Such dynamics can be attributed to rotation-induced reverse switch of the asymmetric magnetic field of the MRPM. The focusing and scattering half-cycles are also accompanied by swirling and reciprocal swirling of the effective working space (see the top view of the **Video S1-3**). The swirling area is found to increase in the order of $\theta = 30°, 45°, 60°$, according to which the gradient components of the magnetic field decrease as the bundle of graphical arrows (indicating magnetic flux) demonstrates (**Figure 3d-f**). Interestingly at the $\theta = 45°$, we observe an additional vector pattern of in-plane swinging with periodic left-right gathering. This distribution is likely caused by the superposition of symmetric magnetic dipoles along the vertical and horizontal axis over one full rotation. Despite the overall decreasing magnetic field strength B (indicated by the vector lengths) as *d* increases, similar dynamics of the magnetic field to the above also appear on all *d* planes. The θ-sensitive magnetic field vector distributions demonstrated here suggest the potential for robust magnetic manipulation of rtPA-Fe_3O_4 swarms. The following experiments will adopt the $\theta = 45°$ configuration unless otherwise specified, which can not only exert magnetic forces on the swarms in a forward manner, but also induce a left-right reciprocating motion of the swarms causing a continuous rubbing effect on the target sample while advancing.

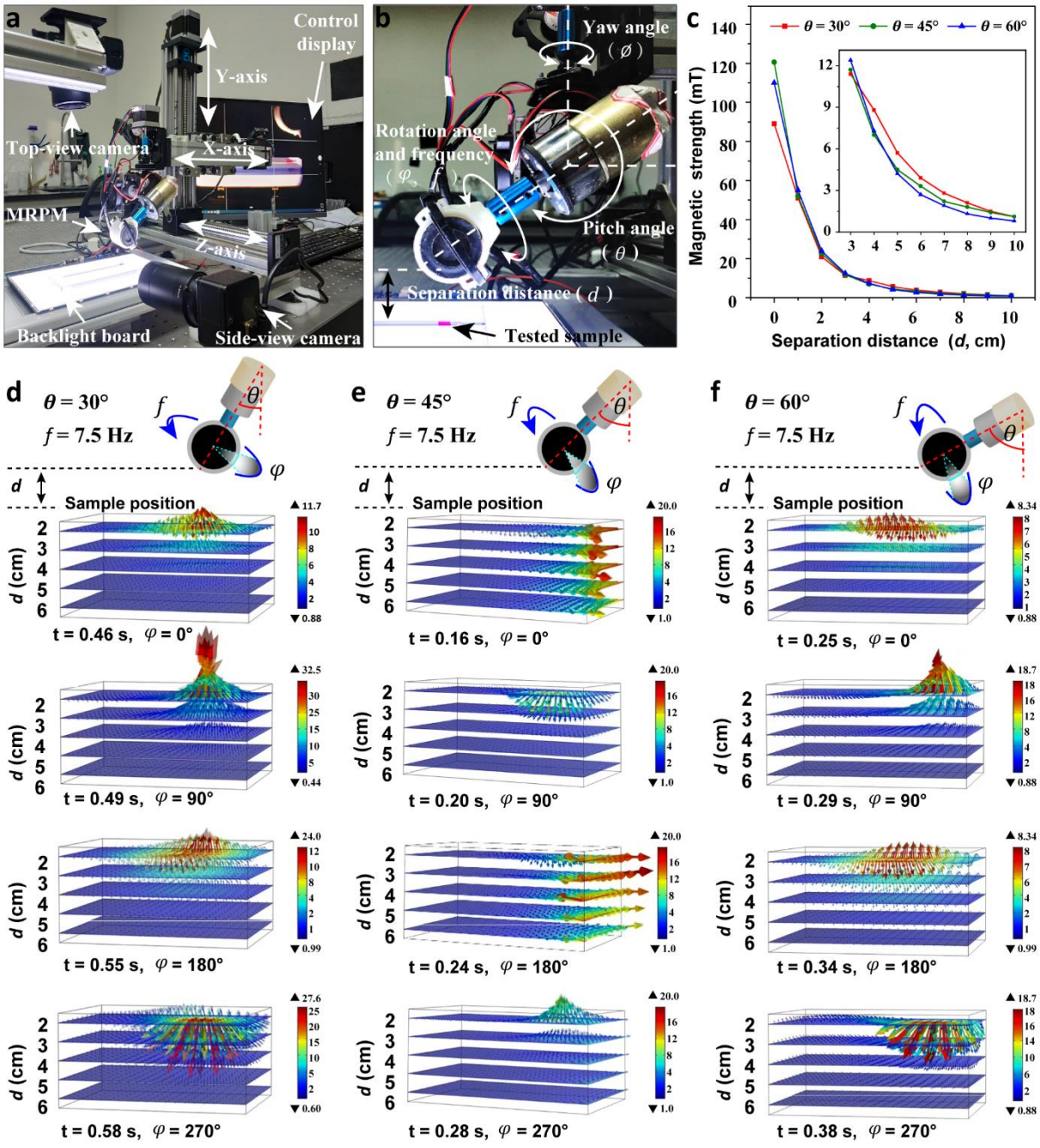

Figure 3. Configuration of the magnetic control system and dynamics of the generated magnetic field. (**a** and **b**) Components of the magnetic control system and manipulation parameters of the permanent magnet mounted on a robotic arm. The workspace below the magnet is for sample loading and magnetic manipulation (more details in "MRPM manipulator" section of the main text). (**c**) Plot of magnetic strength B against separation distance d at pitch angle $\theta = 30°,45°,60°$. The range of d plotted is 0 to10 cm in the main frame, and 3 to 10 cm in the inset. (**d**, **e** and **f**) Dynamic 3-D distribution of the generated magnetic field on horizontal planes at different separation distances for a designated pitch angle $\theta = 30°, 45°, 60°$. The arrow and length of the colored vectors represent the direction and strength of local magnetic fluxes, respectively. The color legend next to each simulation

map illustrates the magnitude of the magnetic vectors, where warmer colors (*e.g.,* red) indicates higher magnetic field strengths.

2.3. Magnetic swarm control

Next, swarming patterns of the rtPA-Fe_3O_4 NPs at $\theta = 30°, 45°, 60°$ are presented for designated values of d and f (**Figure 4a** and **Video S4-6**). Clearly, θ, d and f all play a role in shaping the morphology of the swarm. In general, a small d provides higher B and stronger magnetic forces F_m for assembling the NPs, thus leading to a tighter pattern of the swarm. As d increases, F_m decreases together with B, which results in the swarm patterned in a looser manner or more dispersed state. For f, two opposing effects are observed, depending on the configuration of d. For instance, increasing f at d = 2 cm packs the swarm tighter, whereas at d = 6 cm a looser (or more dispersed) swarm is generated with increasing f. This discrepancy can be attributed to the dynamic balance between a hydrodynamic attractive force (F_{HA}) and a hydrodynamic repulsive force (F_{HR}) acting on the rtPA-Fe_3O_4 chains within the swarm. Both forces are positively correlated with the second power of ω, *i.e.*, $2\pi f$. Under small d, F_{HA} is dominant and would pull individual chains closer to each other upon increasing f, causing the tighter pattern described above. At large d, F_{HR} takes over and contributes to wider gaps between the chains within the swarm at higher f. As for θ, we demonstrate its effect *via* analyzing the force F_{dd} induced by dipole-dipole interactions of magnetized particles. This force could be repulsive ($0° < \theta < 54.7°$) or attractive ($54.7° < \theta < 90°$), depending on the range of θ. Attractive F_{dd} is found to concentrate NPs in the rtPA-Fe_3O_4 suspensions (contributing to a dense swarm at $\theta = 60°$), whereas repulsive F_{dd} scatters the swarm at $\theta = 30°, 45°$ (with a looser pattern for $\theta = 30°$). For more information about the force analysis, please refer to the Supplementary Materials (**Section S2**, **Figure S4-6**, and **Video S7**).

Figure 4b depicts the process of swarm control using a time-lapse sequence (extracted from the **Video S8**). The rtPA-Fe_3O_4 NPs are initially dispersed in phosphate buffer saline (PBS) as a suspension prior to magnetic manipulation (phase Ⅰ, **Figure 4b**). Then based on results in **Fig. 4a**, we set up the magnetic field with parameters (θ, d, f) as (60º, 2 cm, 10 Hz) for assembling the NPs to form a vortex-like swarm (phase Ⅱ, **Figure 4b**). The obtained swarm exhibits robust coupling capable of synchronized motion as instructed by the MRPM. For instance, moving the MRPM forth and back results in the forward and backward motion of swarm, respectively (phase Ⅲ and Ⅳ, **Figure 4b**). By adjusting (θ, d, f) to (45º, 5 cm, 10 Hz), the swarm disassembles into small fragments in a dispersed state and gradually spreads

out as time prolongs (phase V, **Figure 4b**), which indicates a re-dispersion function of the swarm. Similar experiments are performed in fetal bovine serum (**Figure 4c** and **Video S9**), cell culture medium (**Figure 4d** and **Video S10**), urine (**Figure 4e** and **Video S11**) and diluted blood (**Figure 4f** and **Video S12**), and similar patterns are produced. The extensive tests of rtPA-Fe_3O_4 swarms demonstrate their excellent maneuverability in various biofluidic environments. We note that the biological medium's viscosity does affect the assembly and re-dispersion of the swarm. A higher viscosity tends to cause an overall looser pattern of the swarm and a longer time duration for re-dispersion too. This is likely attributed to the increase of viscosity-associated drag force F_D (**Section S2**) and applying higher B and f could circumvent such limitations (when more tightly packed swarms are requested).

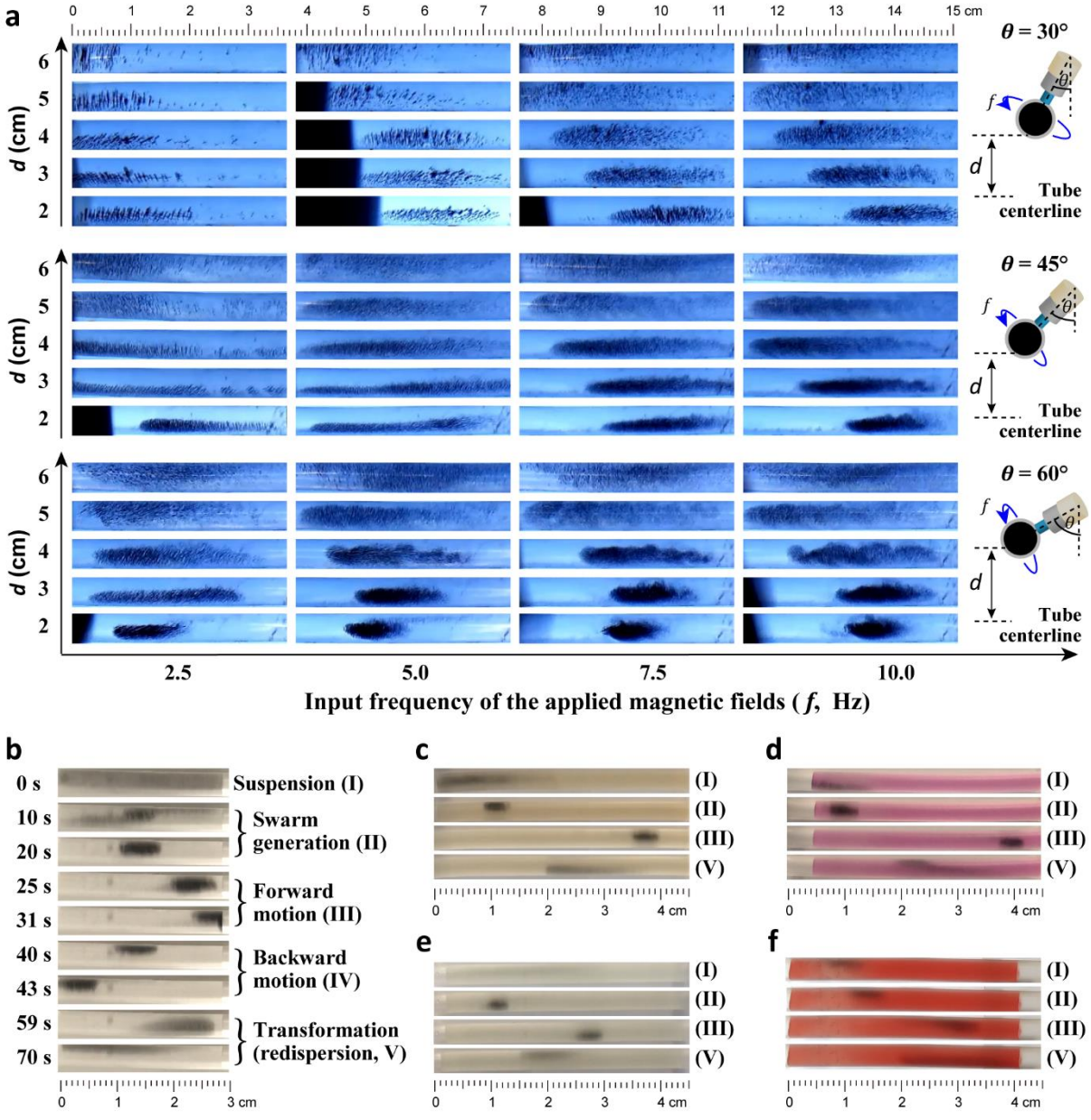

Figure 4. Magnetic manipulation of rtPA-Fe_3O_4 NP swarms. (**a**) Swarmming patterns generated under different combination of parameters (pitch angle θ, separation distances d and input rotation frequency f) of the MRPM in water-filled plastic tubes. The dark zone on the left end of some images are the projected shadow of the magnet. (**b**) Time-lapse image sequence demonstrating the generation and manipulation of a rtPA-Fe_3O_4 swarm in PBS. The whole process includes swarm generation, controlled locomotion and on-demand transformation, for which the corresponding parameter settings of (θ, d, f) are (60º, 2 cm, 10 Hz), (60º, 2 cm, 10 Hz) and (45º, 5 cm, 10 Hz), respectively. The forward and backward locomotion are achieved *via* linear translation of the MRPM. (**c**, **d**, **e** and **f**) Image sequences of rtPA-Fe_3O_4 swarming in fetal bovine serum, cell culture medium, urine and diluted blood, respectively. The same sets of magnetic control parameters are adopted as in (**b**) for PBS.

2.4. Thrombolytic efficacy and ultrasound image tracking

To evaluate the thrombolytic efficacy of the rtPA-Fe_3O_4 swarms, different thrombus types are tested with varying rtPA-Fe_3O_4 concentrations. Experiments below use artificial white blood clots (**Video S13** and **Figure 7**, **section S3**) as a model of thrombus, unless otherwise specified. These clots consist of a cross-linked fibrin protein framework with platelets embedded in it, representative of an early stage of thrombosis[16, 17]. Thrombolytic efficacy is evaluated by the amount of clot removed against the time it takes, where the removal amount of the clot is defined as its reduced volume versus its original state prior to thrombolytic treatment. By this definition, a higher removal amount achieved within less time indicates better efficacy, *vice versa*. According to earlier analyses of the magnetic field mode and swarm control, the magnetic parameters (θ, d, f) are set as (45º, 2 cm, 10 Hz) for potentially optimal thrombolytic performance. **Figure 5a** shows the results in time-lapse sequences, depicting the clot-removal processes under different rtPA-Fe_3O_4 concentrations (for related videos, please refer to **Video S14-15**). Clearly, either increasing the sample concentration or prolonging the treatment time leads to enhanced clot removal. To quantify this enhancing effect, the clot-removal amount at 0.5 h for all concentrations is compared (**Figure 5b**). The enhancement of clot removal appears to gradually level off as the concentration exceeds 500 μg/mL (corresponding to a rtPA concentration of 66 μg/mL, based on the grafting ratio 13.25%), presumably limited by the contact area for the rtPA-Fe_3O_4 NPs and the blood-clot substrate to interact in the test tube. Therefore, the default sample concentration of rtPA-Fe_3O_4 suspension is set as 500 μg/mL for following clot-removal tests, unless otherwise specified.

The clot breakdown capability of the rtPA-Fe_3O_4 swarm observed above can be potentially attributed to three factors acting on the blood clot, namely normal saline immersion, rtPA-enabled enzymatic lysis and swarming-induced mechanical damage[14, 16, 19]. To clarify the contribution of each factor, we monitor and analyze those processes separately (**Figure 5c** and **d**). The results reveal that major contributions are the latter two factors. Interestingly, the sum of clot removal within 0.5 h due to the enzymatic activity of rtPA and the swarming impact of Fe_3O_4 NPs is substantially less than that by an equivalent rtPA-Fe_3O_4 swarm, which achieves a nearly ten-fold efficiency compared to pure rtPA treatment. This clearly suggests a synergistic effect of enzymatic lysis and mechanical damage which markedly enhances the thrombolytic efficacy (the coordination mechanism for which will be uncovered through numerical simulation in the next section). Benefiting from such synergistic effect, the rtPA-Fe_3O_4 swarms also perform well in dissolving red blood clots (**Figure 5e**, **Video S16-17** and **Figure S8**, **section S3.**), which (erythrocyte-abundant) usually occurs after the initial stage of white blood clot formation during thrombosis[16, 17]. To further explore the possibility of ultrasound imaging aimed at *in vivo* thrombolysis using the rtPA-Fe_3O_4 swarms, we first examine the signal intensity against sample concentration, where a positive correlation is observed as expected (**Figure S9**, **section S4**). This is because swarms formed in higher-concentration rtPA-Fe_3O_4 suspensions are likely to assemble more discrete rtPA-Fe_3O_4 NPs into denser clusters and can therefore substantially increase the imaging signal intensity on site. In other words, swarming-enhanced NP concentration brings about stronger ultrasound imaging signal intensity and guarantees real-time tracking of the rtPA-Fe_3O_4 swarm during the clot removal process (**Figure 5f** and **Video S18**), which makes animal tests practical (to be detailed in the following section of "Animal experiments").

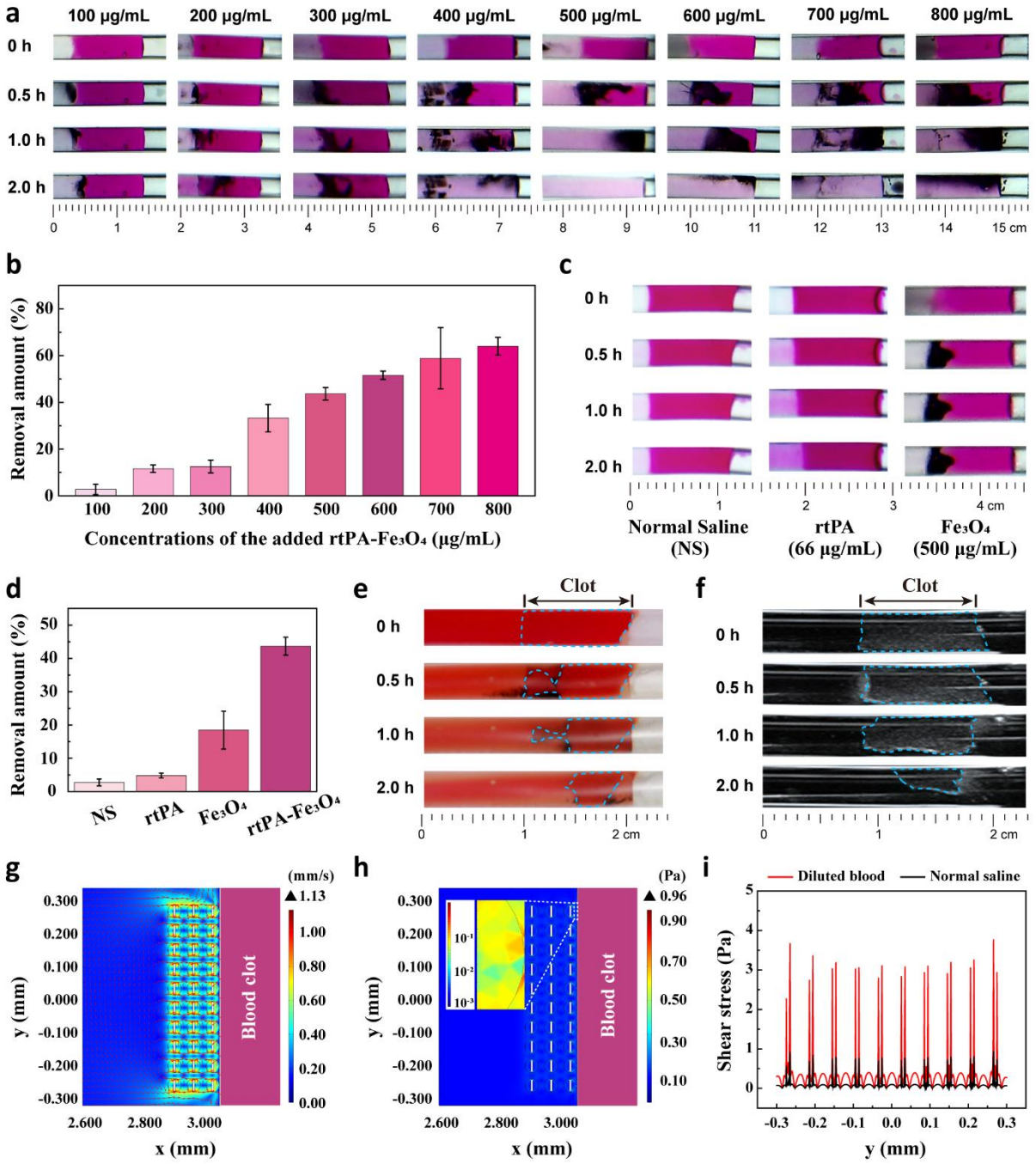

Figure 5. Thrombolytic performance, enzymatic/mechanical synergy and ultrasound imaging of rtPA-Fe_3O_4 swarms. (**a**) Time-lapse image sequences of blood clot removal in a transparent plastic tube filled with normal saline. Rhodamine B dye-doped artificial white blood clots are used in (a-d). The number of rtPA-Fe_3O_4 NPs is evaluated to be 128, 256, 384, 512, 640, 768, 896, 1024 million for 320 μL rtPA-Fe_3O_4 NP suspension samples with concentration 100, 200, 300, 400, 500, 600, 700, 800 μg/mL respectively. (**b**) Quantification of clot removal against sample concentration. The amount of clot removal is calculated at 0.5 h. The error bars represent the standard deviation of three independent experiments (n = 3). (**c**) Time-lapse image sequences of clot removal with normal saline (NS), free rtPA (66 μg/mL) and pure

Fe_3O_4 NPs (500 μg/mL). The equivalent concentration for free rtPA is calculated from the 500 μg/mL solution of rtPA-Fe_3O_4 NPs based on the grafting ratio 13.25%. (**d**) Quantification of clot removal at 0.5 h in solutions of normal saline (NS), free rtPA, pure Fe_3O_4 NPs and rtPA-Fe_3O_4 NPs. The error bars represent the standard deviation of three independent experiments (n = 3). (**e**) Time-lapse image sequence of the removal of a red blood clot (delineated by blue dotted lines) in a transparent plastic tube filled with diluted fresh blood. The rtPA-Fe_3O_4 concentration of is 500 μg/mL, containing an equivalent amount of rtPA at 66 μg/mL. (**f**) Longitudinal ultrasound images of another clot removal process similar to (**e**). The blood clot used in both (e and f) is an artificial red blood clot. (**g, h** and **i**) Numerical analyses of the velocity field, shear stress field and wall shear stress distribution induced by the spinning chains within the rtPA-Fe_3O_4 NP swarm in the vicinity of the blood clot. The X- and Y-axes indicate the horizontal and vertical directions (top view), which represent the distance to the blood clot and the depth along the fluid-clot boundary, respectively.

2.5. Mechanism for synergistic effect of enzymatic lysis and swarming

To understand the enhanced thrombolytic efficacy arising from combined enzymatic and swarming activities of the rtPA-Fe_3O_4 NPs, a closer look at the swarm-clot interface is needed. The flow of an incompressible fluid (*e.g.,* the suspending medium where the swarm is propelled in) can be described by the Navier-Stokes equations,

$$\frac{\partial \boldsymbol{u}}{\partial t} + \boldsymbol{u} \cdot \nabla \boldsymbol{u} = -\frac{1}{\rho}\nabla p + \nu \nabla^2 \boldsymbol{u} \qquad (1)$$

$$\nabla \cdot \mathbf{u} = 0 \qquad (2)$$

wherein **u** represents the velocity field, ρ the fluid density, p the pressure, and ν the kinematic viscosity of the fluid. Given the spherical morphology of the rtPA-Fe_3O_4 NPs (see **Figure 2a-c**), we approximate individual NP chains within the swarm (which are building blocks of the swarm, see **Video S7**) as cylindrical rods for simplicity of modeling. The velocity field **u** induced by rotating NP chains can then be solved using equations demonstrated above through a finite element model (**Figure 5g-5i**), where the average length of individual chains and the inter-chain distance are determined as 36 μm and 25 μm *via* optical microscopy imaging (see **Video S7**). The viscosity and density of the fluid are 4 mPa·s and 1×10^3 kg/m^3 for diluted blood, and 1 mPa·s and 1×10^3 kg/m^3 for normal saline. Rotation frequency of the chains is set according to the MRPM's *f* parameter, in this case, 10 Hz. **Figure 5g** presents the simulated velocity field near the centerline of the tube containing normal saline at a designated time of t = 1 s, where the red arrows indicate flow directions and the background contour map indicates the velocity magnitude. Evidently, a high-velocity region surrounding the swarm emerges due

to local flow perturbations by the spinning NP chains. The induced flows also exert prominent shear stress on the blood clot (**Figure 5h**). A close inspection of the shear stress pattern arising from the NP chain's spinning motion in the vicinity of the blood clot reveals a drastic increase of force magnitudes. Similar flow characteristics to **Figure 5g-5h** are also found in simulations of the swarms in diluted blood **Figure S10**, **section S5**). **Figure 5i** shows the shear stress distribution on the contact line along the blood clot surface, where large fluctuations can be identified and the peak values correspond to locations of the NP chains. Note that for diluted blood and normal saline, the peak shear stresses exerted on the blood clot surface are 0.96 Pa and 3.82 Pa, respectively, both of which are much lower than the shear strength of the prepared clots (36.1 Pa for the white blood clot and 86.1 Pa for the red blood blot, see the **Figure S11** of **section S5**) and are therefore unlikely to tear the clot alone. However, the incorporated rtPA enzyme on the spinning NPs can simultaneously destruct the fibrin framework of the blood clot at the contact surface and locally reduce the shear strength of the clot to potentially comparable levels with the NP chain-induced shear stress[16, 19]. This local reduction of clot strength would aid in mechanical damage imposed by the fluid shear stresses and contribute to accelerated clot removal. Similar enzymatic/mechanical synergy has been demonstrated to overcome mucus barriers *via* integrating bacterium *Helicobacter pylori* with an artificial helical microswimmer[27]. Furthermore, the $\theta = 45°$ configuration of the magnetic field (**Figure 3e**) has implied a left-right reciprocating motion of the swarms that can cause a continuous rubbing effect on the blood clot substrate, which contributes to the breakdown of the blood clot as an extra mechanical factor.

2.6. Biocompatibility test

Biocompatibility of the rtPA-Fe_3O_4 NPs is investigated from three aspects: cytotoxicity, hemolytic behavior and systemic toxicity, which are key indicators to examine before proceeding to *in vivo* testing or clinical trials[2-4, 28]. **Figure 6a** presents the cytotoxicity assays using rtPA-Fe_3O_4 NPs of different concentrations for human umbilical vein endothelial cells (HUEVC). No significant reduction in cell viability can be found against the control group (*i.e.,* concentration 0) after 6 h incubation, even at the maximum concentration of 400 μg/mL (ca. 320 million NPs in 200 μL culture medium). This result is consistent with prior findings of low/negligible cytotoxicity separately reported for rtPA and Fe_3O_4[2-4, 16, 19, 28], which are the two main chemical compositions of our rtPA-Fe_3O_4 NPs. Similar intact cell viability is maintained as the incubation time is prolonged to 24 h (**Figure 6b**), therefore confirming the biosafety of rtPA-Fe_3O_4 NPs to the tested cell line. In hemolysis tests with red blood cells, low-

level hemolysis (< 3%) is found even at the highest concentration tested, *i.e.,*1000 μg/mL (**Figure 6c**). This indicates the safety of rtPA-Fe_3O_4 NPs for long-term retention in the blood stream, which is highly desired for intravenous drug therapy. Systemic toxicity is also assessed with a relatively high dosage (10 mg/kg for 20 g body weight) in male Balb/c mice. No accidental death or significant loss of the body weight (**Figure S12**, **section S6**) occurs during the assessment. Further histological analysis of the heart, liver, spleen, lung and kidney reveals no evident difference between the tested and control groups, either (**Figure 6d**). Additionally, biochemical analysis is conducted to examine the tested mouse's blood plasma extracted from fresh blood. Typical biomarkers of the kidney function (blood urea nitrogen, BUN, normal: 10.81-34.74 mg/dL; creatinine, CR, normal: 10.91-85.09 μmol/L) are all found at normal levels (**Figure 6e**), and similar findings for the liver function biomarkers (alkaline phosphatase, ALP, normal: 22.52-474.35 U/L; serum alanine transaminase, ALT, normal: 10.06-96.47 U/L; aspartate aminotransferase, AST, normal: 36.31-235.48 U/L; **Figure 6f**). All biocompatibility test results, taken together, suggest that the rtPA-Fe_3O_4 NPs are of favorable biocompatibility and can be applied for further *in vivo* developments using animal models.

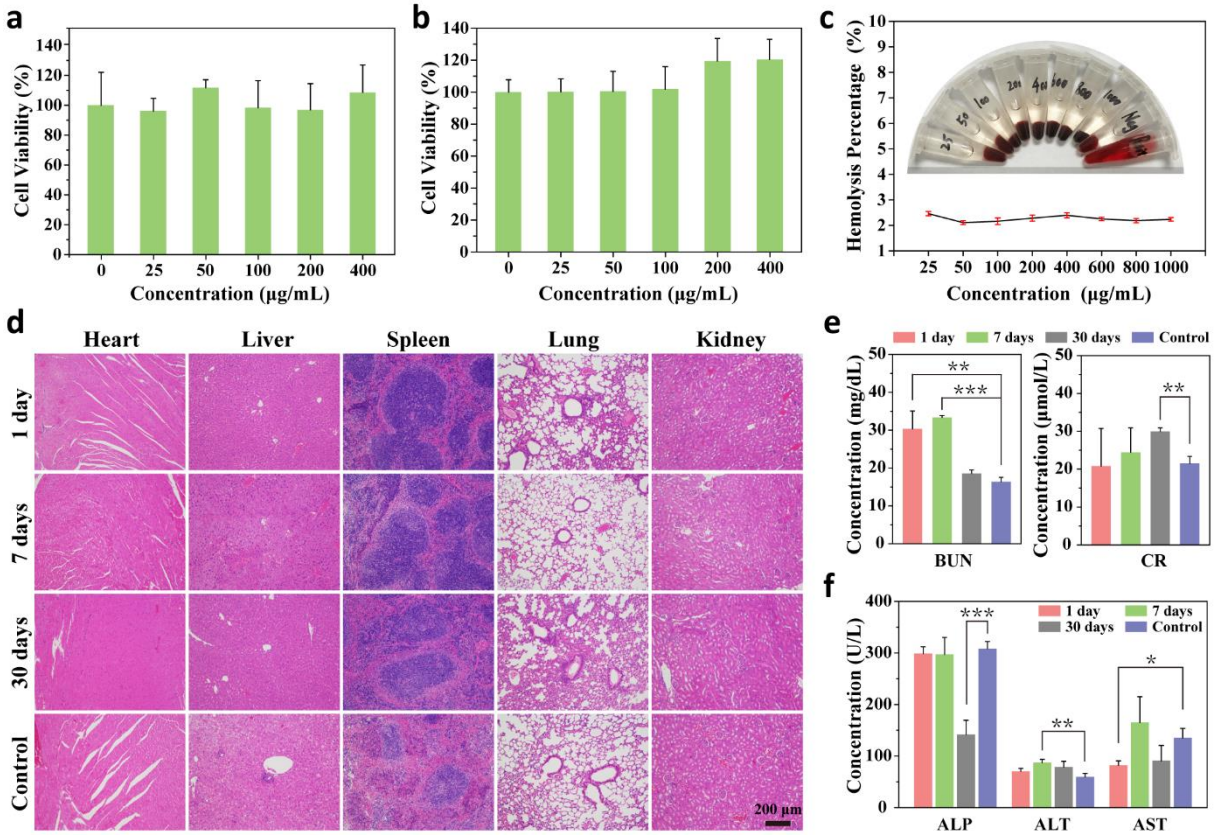

Figure 6. Biocompatibility of rtPA-Fe_3O_4 NPs. (**a** and **b**) Relative viability of the HUEVC cell line cultured with rtPA-Fe_3O_4 of varying concentration for 6 h and 24 h, respectively (n = 3). No viability reduction of statistical significance is found. (**c**) Hemolytic behavior of rtPA-

Fe_3O_4 NPs at different sample concentrations (n = 3). The inset shows the samples after the hemolysis assay, where the supernatant and dark-red precipitation suggests low hemolysis. (**d**) Histological photomicrographs of main organ tissues from the mice subject to tail vein administration of 0.2 mg rtPA-Fe_3O_4 NPs (experimental group) and equivalent amount of normal saline (control group). All panels share the same scale bar, 200 μm. (**e** and **f**) Concentration of key biomarkers indicating kidney function and liver function, respectively. The data are presented as mean ± standard deviation of three independent experiments (n = 3, $*P < 0.05$, $**P < 0.01$ and $***P < 0.001$). In (a, b and c), the number of rtPA-Fe_3O_4 NPs in the solution can be calculated based on the sample concentration and volume. In (d, e and f), Histological analysis for the control groups is at day 30.

2.7. Animal experiments

In our study, *in vivo* animal testing is conducted in a carotid artery occlusion model of New Zealand white rabbits, where a blood clot is introduced with the aid of a catheter. The choice of this animal model has three considerations. First, blood clot-induced carotid artery occlusion represents one major cause of stroke[34], for which fast thrombolysis is imperatively needed. Second, the anatomic structure of carotid artery features long vessel segments with few vascular branches and is therefore suitable for initial demonstration of magnetically-controlled NP swarming *in vivo* as feasibility test[35]. Third, the construction of this animal model is straightforward and has a high success rate. **Figure 7a** depicts the experimental setup, where the MRPM is located above the carotid artery for magnetic manipulation and a digital surgical microscope is equipped for process monitoring. To enhance the imaging quality, we also place a backlight board next to the exposed carotid artery (**Figure 7b-d**). 30 μL rtPA-Fe_3O_4 NP suspension with a concentration of 5 mg/mL (corresponding to ca. 600 million NPs and a rtPA dosage/body weight ratio of 7.95 μg/kg) is injected into the carotid artery *via* a catheter. Then magnetic control procedures as in section "Magnetic swarm control" are applied to perform designated manipulation of the rtPA-Fe_3O_4 NPs such as locomotion, transformation and removal as presented in **Figure 7b-d** (extracted from the **Video S19**), which suggests robust maneuverability of rtPA-Fe_3O_4 swarms in the blood vessel. According to previous *in vitro* tests, the MRPM parameters as set as (θ, d, f) = (45°, 2 cm, 10 Hz) for *in vivo* demonstration, which are expected deliver thrombolysis efficacy. By tuning the MRPM's motion, we guide the rtPA-Fe_3O_4 swarm towards to the clot's location (**Figure 7e-f** and **Video S20**), and then trigger the thrombolysis process. The thrombolysis process is found highly effective (**Figure 7f-g** and **Video S20**), only taking about 19 min for the elongated clot of cylindrical shape (diameter 1.42

mm, height 4.20 mm) to be removed. This suggests a large potential of fast thrombolysis *in vivo* using our rtPA-Fe_3O_4 swarms. Furthermore, ultrasound images as shown in **Figure 7h-j** (extracted from the **Video S21-23**) capture the thrombolysis process, where location and size of the artery, the clot and the swarm can be clearly distinguished. The ultrasound imaging capacity depict a pathway towards reliable *in vivo* monitoring of thrombolysis treatment by injected rtPA-Fe_3O_4 swarms. Additionally, we inspect cross-sectional slices of the carotid artery with histological analysis, aimed at assessing the effect of swarming-induced mechanical damage on the vascular inner wall. **Figure 7k-m** present histological characteristics of vessel samples subject to swarm locomotion and/or clot removal. Apart from occasional rtPA-Fe_3O_4 NPs and residual clot fragments inside the carotid artery, all sample's inner walls are intact and the endothelial cells manifest normal morphology, therefore suggesting negligible vascular damages. All brought together, our animal testing demonstrate that the rtPA-Fe_3O_4 NP swarms are envisioned for practical *in vivo* trials of imaging-guided fast thrombolysis.

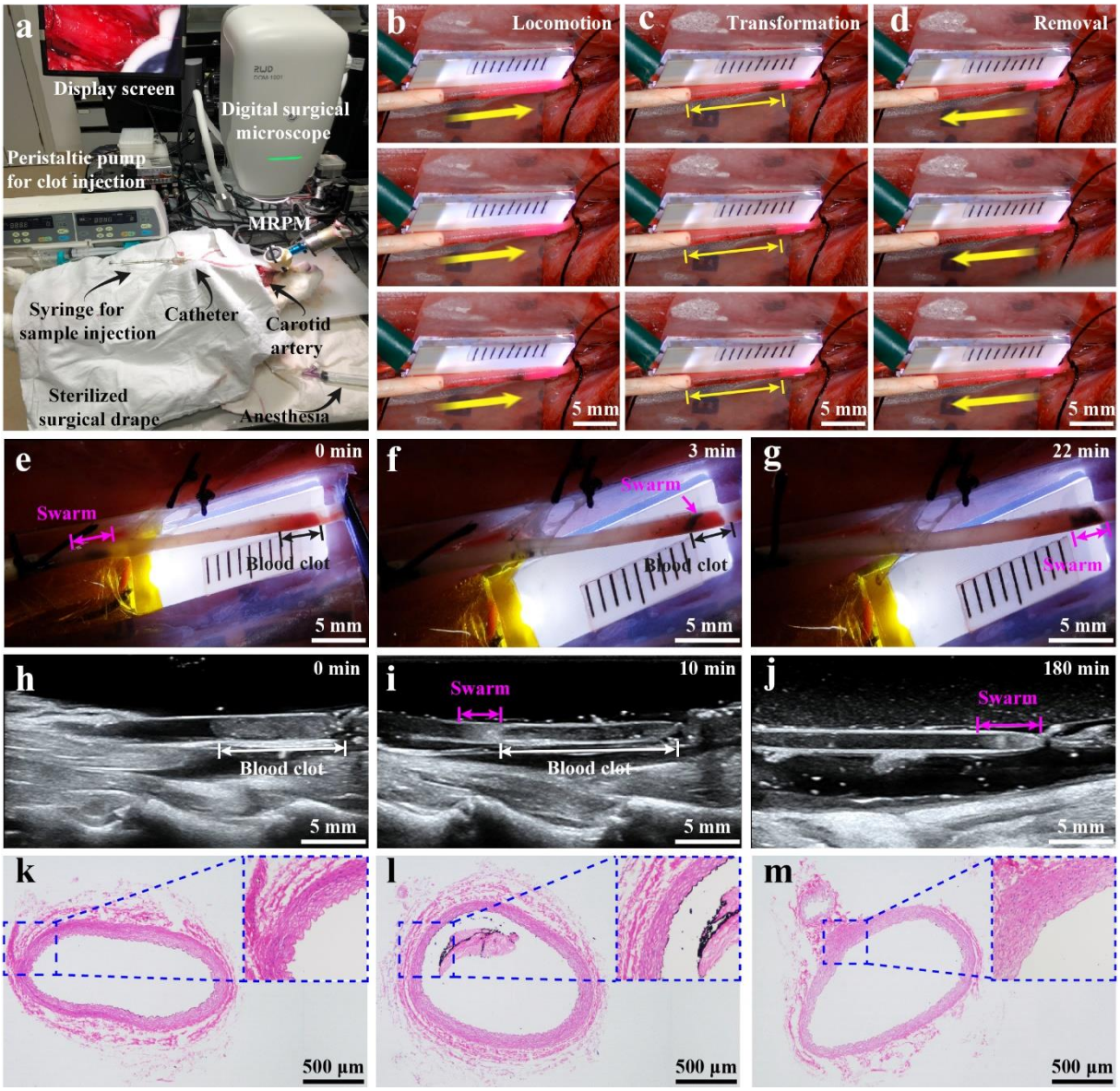

Figure 7. Magnetic control and thrombolytic performance of rtPA-Fe_3O_4 swarms in a rabbit carotid artery occlusion model. (**a**) Digital photograph of the experimental setup with animal loaded. One end of the catheter is inserted to the carotid artery, while the other end of it is connected to the syringe and peristaltic pump. (**b**, **c** and **d**) Time-lapse sequences illustrating magnetic control of the swarm for its locomotion, transformation and removal. All images (extracted from **Video S19**) share the same scale bar, 5mm. The carotid artery is placed next to a backlight board for visual clarity. The one-way arrows (yellow) indicate the direction of the swarm's locomotion. The one two-way arrows (yellow) indicate the range of the swarm's transformation in space. On the left-hand side of carotid artery is the inserted catheter (milk-white color) and an electric cable (in green color) for powering the backlight board. (**e**, **f** and **g**) Time-lapse sequence of *in vivo* thrombolysis using the rtPA-Fe_3O_4 swarm (video available in **Video S20**). (**h**, **i** and **j**) Longitudinal ultrasound images (extracted from **Video S21-23**)

monitoring the thrombolytic process in real-time. (**k**, **l** and **m**) Histological photomicrographs of different vessel segments sliced from the rabbit carotid artery after the experiment. The segment in (k) only experienced the rtPA-Fe_3O_4 swarm's locomotion. The segments in (l and m) correspond to location of the injected blood clot during and after the thrombolytic process, respectively.

3. Conclusion

In this study, we report an integrated platform aimed at *in vivo* thrombus therapy, which features a boosted therapeutic efficacy arising from synergistic effect of functionalization/swarming of magnetite nanoparticles. The facile synthesis of rtPA-Fe_3O_4 NPs is a two-step process through hydrothermal reaction and EDC/NHS-based treatment. A Fe_3O_4 matrix incorporating rtPA modification endows the synthesized NPs with multiple superior functions, one being enzyme-triggered lysis of thrombus enabled by the integrated rtPA activity. To preform practical magnetic manipulation and swarm control of rtPA-Fe_3O_4 NPs applicable to animal experiments, a customized maneuverable rotating permanent magnet (MRPM) system is constructed and comprehensively characterized through numerical simulations. The MRPM system not only supports the generation of inhomogeneous rotating/gradient magnetic fields, but also possesses high-level operation flexibility and large working space. Actuated and controlled by the MRPM, the rtPA-Fe_3O_4 NPs are capable of forming millimeter-scale swarms in various patterns, depending on the magnetic stimuli they receive. On the one hand, the generated swarms demonstrate robust maneuverability in biofluids to perform synchronized spinning motion, on-demand transformation and controlled 3-D propulsion, therefore holding promise for applications in complex microenvironments such as the vascular network. On the other hand, the rtPA-Fe_3O_4 swarms exhibit enhanced imaging signals that can guarantee reliable *in vivo* tracking *via* ultrasound imaging, which is a necessity for precise treatment of thrombus on site. The swarm spinning-induced shear stresses exerted on the target thrombus constitute a continuous mechanical damage contributing to thrombolysis. Such mechanical damage, combined with the rtPA enzymatic efficacy, leads to a pharmacomechanical synergistic effect that achieves efficient thrombolysis in a rabbit carotid artery occlusion model. To conclude, this work establishes a novel strategy for integrating functions and proposes an injectable thrombolytic nanomedicine that incorporates intravenous drug therapy and robotic intervention.

4. Discussion

In the field of thrombus therapy, current research works mainly focus on developing new drugs and suitable drug carriers[14, 21, 22, 24, 29, 30], introducing proper physical stimuli (*e.g.,* localized hyperthermia and ultrasound blasting microbubbles)[31, 32, 33], and improving surgical protocols or interventional tools[20, 33]. Micro-/nanomotors, an active matter capable of converting chemical/physical energy into propulsion power at low Reynolds number, represent an alternative delivery/therapeutic agent with promising applications[14, 21, 22, 30, 32]. Recent progress features the development of conceptual proofs using light-driven or magnetically-actuated nanomotors to accelerate thrombolysis, relying on active delivery of drug agents and/or motor-mediated fluid forces. The mechanisms for these nanomotors include enrichment of drug concentration on site, more effective attachment/diffusion/penetration of drug into the thrombus and additional mechanical destruction of the thrombus structure. One exemplar application of light-driven nanomotors for thrombus therapy was demonstrated by Wan *et al.*[30], who constructed porous silica/platinum spherical nanomotors for loading thrombolytic drugs and anticoagulant heparin within, with external camouflage of a layer of platelet membrane. During circulation in the blood stream, the special proteins on the platelet membrane target the thrombus site and contribute to localized enrichment of the nanomotors, which can then realize sequential release of thrombolytic/anticoagulant drugs with the aid of near-infrared (NIR) light irradiation that heats the platinum nanoparticles and destroys the platelet membrane. A more recent work by Deng *et al.* designed a polydopamine (PDA) nanomotor with nitric-oxide (NO) donors loaded, which can penetrate deep into the thrombus via the propulsion effect of NO released on site upon NIR light irradiation[32]. Combining mechanical and photothermal thrombolysis, the work not only realized nonpharmaceutical thrombus therapy, but also held promise for preventing thrombus recurrence after the treatment thanks to the role of the released NO in antiplatelet adhesion as well as vasodilation regulation. Both works above on light-driven nanomotors have been tested in animals and demonstrated higher or comparable efficacy than clinical thrombolytic drugs. However, the limited penetration depth of the near-infrared light may limit the clinical translation of such nanomotors towards practical treatment of patients.

As for magnetically-actuated nanomotors, Cheng *et al.* managed to double the thrombolytic efficacy of tPA drugs by accelerating their diffusion on thrombus site through rotating Nickle nanorods[21] (in a following work, Fe_3O_4 nanorods were used by the authors to overcome the poor biocompatibility of Nickle material[22]). The enhanced treatment of thrombus was further verified in a rat embolic model. Nevertheless, the tPA concentration used for the *in vivo* experiments was 10 mg/kg (expressed as drug dosage/animal body weight), much

higher than the clinical dosage 0.9 mg/kg, whereas treatment using high tPA dosages is known to cause adverse effects, e.g., bleeding. More recently, Wang *et al.* harnessed a microswarm of Fe_3O_4 nanoparticles to assist the tPA-mediated thrombolysis, which were capable of reconfigurable morphology and can be tracked via ultrasound imaging[14]. However, the thrombolysis rate was only moderately higher (ca. 2.5 times) than using free tPA, and the concentration of tPA used (30 mg/mL) was still too high compared with the equivalent clinical dosage (10.5-14.5 μg/mL, converted from of 0.9 mg/kg). In our study, where rtPA is integrated onto Fe_3O_4 nanoparticles, a drug concentration of 66 μg/mL is sufficient for in vitro experiments and that for animal experiments is only 7.95 μg/kg (corresponding to a concentration in blood of 0.128 μg/mL), with a ten-fold thrombolytic efficiency achieved in comparison to pure rtPA treatment. Given all discussed above, the prospects of applying our developed rtPA-Fe_3O_4 swarms for clinical thrombus therapy are bright, with their operation feasibility, material biocompatibility, thrombolytic efficacy and real-time tracking comprehensively examined. That being said, more preclinical trials are needed and it is not straightforward to realize large-scale clinical translation towards practical therapeutics for patient treatment. Our following work will commit to constructing multi-modal *in vivo* imaging for real-time, noninvasive and high-resolution tracking of the swarms in blood stream, as well as conducting abundant preclinical trials in animal models.

5. Materials and Methods

Materials: Ferrous chloride hexahydrate ($FeCl_3 \cdot 6H_2O$), sodium citrate, sodium acetate, ethyl alcohol, and ethylene glycol were purchased from the Aladdin (China). N-Hydroxysuccinimide (NHS), N-(3-Dimethylaminopropyl)-N'-ethylcarbodiimide hydrochloride (EDC), 3-(4, 5-dimethythiazole-)2-yl-2,5-diphenyltetrazolium bromide (MTT), dimethyl sulphoxide (DMSO) and Rhodamine B were purchased from the Sigma-Aldrich (USA). Recombinant tissue plasminogen activator (rtPA) was purchased from the Boehringer Ingelheim (Germany). Protease substrate H-DIsoleucyl-L-prolyl-L-arginine-p-nitroaniline (S-2288) was purchased from the Chromogenix (Italy). Human plasma thrombin was purchased from the Shanghai Yeasen BioTechnologies Co., Ltd. (China). Roswell park memorial institute (RPMI 1640) medium, trypsin solution and phosphate buffer saline (PBS) were purchased from the Hyclone (USA). Fetal bovine serum, streptomycin and penicillin were purchased from the Gibco (USA). Normal saline was purchased from the Chenxin Pharmaceutical Co., Ltd. (China). All chemical/biological reagents were directly used for our

experiments unless otherwise specified. Deionized (DI) water was prepared on a PURELAB Option instrument of the ELGA LabWater (UK).

Hdrothermal synthesis: Hydrothermal synthesis of the Fe_3O_4 NPs employed a previously reported protocol[2, 23]. The reactants $FeCl_3 \cdot 6H_2O$ (1.35 g), sodium acetate (3.6 g) and sodium citrate (1.0 g) were sequentially added to a 40 mL ethylene glycol, followed by continuous magnetic stirring for 30 min. The obtained mixture was transferred into a 50 mL teflon-lined stainless-steel autoclave (Nanjin Zhengxin Instrument Co., Ltd., China). For hydrothermal reactions, the autoclave was sealed and heated at 200 °C for 24 hours. Black COOH-Fe_3O_4 NPs were then collected via magnetic attraction after the autoclave's temperature dropping to room temperature. They were washed three times using absolute ethanol and re-suspended in PBS solutions for storage.

Drug loading and rtPA grafting ratio: The EDC/NHS treatment was carried out in a 40 mL DI water containing Fe_3O_4 NPs (10 mg), EDC (40 mg) and NHS (48 mg) at room temperature. Continuous mechanical stirring (300 rpm) was applied for 2 hours via a mechanical agitator purchased from the Shanghai Beilun Instrument Co., Ltd. (China). The obtained Fe_3O_4 NPs were washed three times with DI water and re-suspended in PBS for subsequent rtPA grafting. Before being used for the grafting, commercially available rtPA products were further purified to remove the L-arginine (one amino acid probably affecting the grafting of rtPA). For purification, the lyophilized rtPA powders (186.64 mg) were dissolved in 8.0 mL PBS and transferred into an Amicon® Ultra ultrafiltration tube (MW = 30 kD, Millipore Corporation, USA) at 4°C. The desired rtPA was collected via centrifugation (10,000 g, 30 min, 4°C) on a Eppendorf refrigerated centrifuge. The obtained rtPA, dissolved in 8.0 mL PBS with a concentration of 0.5 mg/mL, was immediately added to the EDC/NHS-treated Fe_3O_4 suspension (32 mL, 10 mg Fe_3O_4 NPs). The grafting process was completed at 4°C under continuous mechanical stirring of 300 rpm lasting for 3 hours. The collected rtPA-Fe_3O_4 NPs were then washed clean and stored in PBS for subsequent experiments.
The drug loading percentage, or grafting ratio of rtPA was calculated as following:

$$\text{grafting ratio } (\%) = \frac{\text{mass of grafted rtPA}}{\text{mass of grafted rtPA} + \text{mass of } Fe_3O_4 \text{ NPs}} \times 100\% \qquad (3)$$

wherein the mass of grafted rtPA (mg) was calculated by subtracting the total amount of added rtPA by the amount of residual rtPA in the supernatant solution after the grafting process. To

determine the amount of residual rtPA, a human tissue-plasminogen activator immunoassay ELISA kit (Dogesce, China) was used to measure the concentration of residual rtPA through an absorbance-concentration standard curve (acquired at 450 nm) (**Figure S2, section S1**). The residual rtPA amount can then be calculated as the product of rtPA concentration and solution volume.

Structural characterization: SEM images were acquired at an accelerating voltage of 10 and 200 kV on a JSM-7800F scanning electron microscope (JEOL, Japan), while TEM images at 200 kV on a JEOL JEM 2100 transmission electron microscope. Elemental mapping analysis was conducted with a talos F200X energy-dispersive X-ray spectrometry mounted on TEM instrument. The accelerating voltage of mapping was set at 20 kV. Size distribution and zeta potential were measured on a Zetasizer Nano ZS90 dynamic light scattering instrument (Malvern, UK). XRD pattern was recorded using a Rigaku Ultima IV X-ray diffractometer (Hitachi, Japan). The operating voltage and current were 40 kV and 40 mA, respectively. Magnetic properties were characterized at room temperature with a vibrating sample magnetometer (LakeShore7404, USA). Fourier Transform infrared (FTIR) spectroscopy was investigated on a Thermo Scientific Nicolet iS5 (resolution, 4 cm^{-1}). All tested samples of FTIR were embedded in KBr pellets. The testing range was set between 400 and 4000 cm^{-1}.

Enzyme activity assay: Enzyme activity was evaluated following the protocol previously reported[40, 52]. Tested samples included the rtPA-Fe_3O_4 NPs, Fe_3O_4 NPs and fresh rtPA. The Fe_3O_4 NPs and fresh rtPA were used as the control groups. As the first step of testing, the diluted samples (200 μL) were added to Tris-NaCl buffers (0.1 mM, 200 μL) and subject to a mixing for 4 min. Subsequently, the chromogenic subtract S-2288 (1 mM, 200 μL) was added at 37°C environment. After incubation for our designated time duration, the mixture was transferred to a 96-well plate for light absorbance measurement. The light absorbance was measured at 405 nm on a Thermo Scientific Multiskan GO spectrophotometer. The change rates of the absorbance-time curves represented enzyme activity level. High rates indicated high enzyme activity level, vice versa.

Conversion between rtPA-Fe_3O_4 concentration and nanoparticle number: The concentration c (μg/mL or mg/mL) of rtPA-Fe_3O_4 NPs dispersed in suspension was calculated by dividing the total added mass M_{total} (g) of rtPA-Fe_3O_4 by the solution volume V_s (L). The mass of an individual rtPA-Fe_3O_4 NP M_{np} (g) can be calculated as its density ρ (g/cm^3) multiplied by its

volume V_f (cm^3). According to the electron microscope imaging, each rtPA-Fe_3O_4 NP can be considered as a microsphere with an diameter d of ca. 452 nm (or $\mathbf{4.52 \times 10^{-5}}$cm to match the density unit) and a volume V_f of $\mathbf{^4/_3\,\pi(d/2)^3}$. Given the dominant mass of Fe_3O_4 in rtPA-Fe_3O_4, the density ρ can be further approximated by that of Fe_3O_4 (i.e., 5.18 g/cm^3). The number N of rtPA-Fe_3O_4 NPs in the suspension was then estimated as M_{total} divided by M_{np} according to the formula below:

$$N = \frac{M_{total}}{M_{np}} = \frac{cV_s}{5.18\times{}^4/_3\pi\times(2.26\times10^{-5})^3} \quad (4)$$

Magnetic manipulation and swarm control: Magnetic manipulation of the rtPA-Fe_3O_4 NPs was carried out in a transparent plastic tube placed under the MRPM. The tube was made of polyvinyl chloride (PVC) and had an inner diameter of 3 mm. Fluidic media including water (175 μL), normal saline or PBS (175 μL), fetal bovine serum (325 μL), cell culture medium (300 μL), urine (325 μL), diluted blood (250 μL) together with rtPA-Fe_3O_4 NPs (5 mg/mL) were injected into the tubes using syringes for different experiments. The blood was extracted from a rabbit and diluted ten times with PBS. The protocols of blood sampling were approved by the Animal Care and Use Committee of Shanghai Jiaotong University affiliated Shanghai sixth people's hospital, the People's Republic of China. Before being injected, the rtPA-Fe_3O_4 NPs were all dispersed in PBS. Related videos were recorded using the CMOS camera described in "Construction and numerical simulation of MRPM manipulator".

Assessment of thrombolytic efficacy: Experiments were conducted in transparent plastic tubes (inner diameter 3 mm, length 12 cm). To prepare the white blood clot, human thrombin (1000 U/mL, 10 μL) and a small amount of Rhodamine B dye was added to 50 μL platelet rich plasma (taken from a rabbit). The role of Rhodamine B was to stain the clot so the clot is visible under camera. After being mixed by a vortex, the obtained mixture was immediately transferred to the tubes and incubated at 37 °C for 2 hours. The prepared clot, about 10 mm in length, was tightly adhered to the tube's inner walls. For testing, the clot-filled tubes were placed flat beneath the MRPM. The mixture of rtPA-Fe_3O_4 NPs and normal saline (425 μL) was carefully injected to the tubes using syringes. In the experiments of red blood clots, normal saline used above was replaced with diluted blood. The red blood clots were prepared in the whole blood without the addition of Rhodamine B.

Ultrasound imaging: Samples used to quantify the relationship between rtPA-Fe_3O_4 NP number (or concentration) and ultrasound imaging signal were dispersed in DI water and placed in centrifuge tubes of 1.5 mL. To avoid interference from the air, these tubes were dipped in water for the imaging tests. For in vitro and in vivo monitoring of thrombolytic processes, the screening of the air noises applied the ultrasonic couplant (Ambition T. C., China). Both ultrasound images and related videos were captured on a Mindray ultrasonic imaging system (Resona 7) using the L20-5U transducer. Center frequency, intensity power and contrast gain were set as 12.5-23.0 MHz, 10%, and 40 dB, respectively.

Cytotoxicity assay: Cytotoxicity was measured with 3-(4, 5-dimethythiazole-)2-yl-2,5-diphenyltetrazolium bromide (MTT) assays[3, 4]. The HUVEC cells were cultured in 10 cm plastic tissue culture dishes (Corning Incorporated, USA) and placed at 37°C under a humidified air atmosphere of 5% CO_2. The RPMI 1640 medium containing 10% fetal bovine serum, 100 g/mL streptomycin and 100 g/mL penicillin was applied for the culture. At the cell confluence of ca. 75%–80%, they were collected via centrifugation and then re-suspended in fresh culture medium. The suspension was seeded in 96-well plates (ca. 4000 cells per well) and incubated overnight, with the cell density reaching ca. 1×10^4 per well. The sterilized rtPA-Fe_3O_4 NPs were dispersed in fresh culture media. These samples were added as six replicate wells for each concentration. The concentrations of samples were 0, 25, 50, 100, 200 and 400 μg/mL in 200 μL culture medium, including 0, 20, 40, 80, 160, and 320 million NPs. After incubation for 6 and 24 hours, the MTT reagent (5 mg/mL, 50 μL) was added to each well, followed by additional 4 hour incubation. The supernatant of each well was carefully removed, and dimethyl sulphoxide (DMSO, 150 μL) was added. With a horizontal shaker (IKA, KS260 B S25, Germany), the formazan precipitates were gradually dissolved. The absorbance of the tested solution was directly read on a Thermo Scientific Multiskan GO microplate reader at 490 nm. Cell viability was then calculated from the absorbance values.

Hemolytic behavior: The red blood cells (RBCs) were collected from fresh blood of a rabbit via centrifugation (1500 rpm, 10 minutes). The obtained pellets were re-suspended in PBS, with their weight percentage reaching ca. 2%. Tested samples were 0.5 mL rtPA-Fe_3O_4 NP PBS suspension at a concentration of 50, 100, 200, 400, 800 and 1000 μg/mL (equivalent to 100 million, 200 million, 400 million, 800 million, 1.6 billion and 2 billion NPs, respectively). DI water and PBS of equivalent volume was set for the control groups. All used

samples were mixed with 0.5 mL RBC suspension and incubated at 37°C for 30 minutes. To gain the supernatant, the mixture was subject to centrifugation (2500 rpm, 5 min). Digital photos were taken with the camera mounted on a phone. The absorbance of the supernatant was directly read at 540 nm from a Multiskan GO microplate reader (Thermo Scientific, USA). Hemolysis rate was calculated according to the following formula:

$$\text{Hemolyis rate (\%)} = \frac{\text{Absorbance of tested sample} - \text{Absorbance of PBS}}{\text{Absorbance of DI water} + \text{Absorbance of PBS}} \times 100\% \quad (5)$$

Systemic toxicity assessment: Following the literature[4], male Balb/c mice (4-6 weeks old, ca. 20 g body weight per mouse) were chosen as a model animal for the test of systemic toxicity. They were divided into six groups, with three mice in each group (n = 3). The rtPA-Fe_3O_4 suspensions (5 mg/mL, 0.04 mL), dispersed in normal saline and containing 0.2 mg rtPA-Fe_3O_4, were delivered into the tail veins of nine mice (three groups) via intravenous injection. Equivalent normal saline was injected to the mice in the control group. After being bred for 1, 7 and 30 days, the blood samples used for biochemical analysis were collected from the orbital venous of mice, and these mice were euthanatized to obtain heart, liver, spleen, lung and kidney organs. Biomarkers of the liver function (i.e., ALT, AST and ALB) were quantified with enzyme-linked immunosorbent assay (ELISA) kits (Beyotime, China), whereas biomarkers of the kidney function (i.e., BUN and Cr) using the BUN assay kits and Cr assay kits (Nanjing Jiancheng Bioengineering Institute, China). All the collected organs were conserved in 4% paraformaldehyde solution for hematoxylin-eosin (H&E) staining. All processes of H&E staining were commissioned to the SCIGE Company (China). The optical images of histological analysis were acquired with an OLYMPUS optical microscope (Nikon eclipse E 100, Olympus Corporation, Japan).

Animal experiments: Animal occlusion models were constructed using New Zealand white rabbits (male, a mass of ca. 2.5 kg) purchased from the Shanghai SLAC Laboratory Animal Co., Ltd. (China). All the procedures regarding animal maintenance and experiments are in strict accordance with the policy of the Institutional Animal Care and Use Committee of Shanghai Jiaotong University affiliated Shanghai sixth people's hospital. Anesthesia was performed by intravenous injection of pentobarbital sodium solution (3%, 1 mL/kg). The sterilized surgical drape was applied to keep the anesthetized rabbit warm and clean. To prepare the red clot, its autologous whole blood (about 0.1 mL) was slowly drawn from the auricular vein and delivered into a tube containing thrombin of 100 units. Next, the rabbit's

left carotid artery was fully exposed by an incision of the neck skin. Proximal portion of the carotid artery was ligated with a suture, where a medical catheter was then inserted into the vessel. With the aid of a peristaltic pump coupled to the catheter (see Figure 7a), the as-prepared clot (mixed with 1 mL normal saline) was slowly injected to the left carotid artery. The blood clot-induced carotid artery occlusion model was successfully constructed as the suture ligation of distal vessel accomplished. For histological analysis, the experimented rabbits were sacrificed and their carotid artery located at different regions were dissected. Subsequent processing of the collected fragments followed the procedure as in "Systematic toxicity assessment".

Statistical analysis: Quantitative data in this study were expressed as the mean ± standard deviation (SD). Statistical analysis was conducted with the independent-samples T test and one-factor ANOVA test. Probability (P) values were used to assess statistical significance, assigned at $*P < 0.05$, $**P < 0.01$ and $***P < 0.001$. All statistical analyses were performed with IBM SPSS 16.0.

Supporting Information

Supporting Information is available from the Wiley Online Library or from the author.

Acknowledgements

The authors thank Dr. Ying Zhang (Department of Obstetrics and Gynaecology, Wuhan University) for assisting animal experiments, and Prof. Dongxu Zhang, Mr. Fei Duan, Mr. Yanghui Chen and Mr. Juntian Zeng (School of Public Health, Xiamen University) for offering 3-D printing instruments and supporting the use of them. This project was supported by the NSFC Key Projects of International Cooperation and Exchanges (81720108023), the NSFC Key Project (82030050), the National Key R&D Program of China (2018YFC0115200), the Fundamental Research Funds for the Central Universities of China (20720190076), the Opening Project of Guangdong Provincial Key Lab of Robotics and Intelligent System (XDHT2019588A), and the National Natural Science Foundation of China (82001845). X. T., P. L. and Q. Z. contributed equally to this work.

Received: ((will be filled in by the editorial staff))
Revised: ((will be filled in by the editorial staff))
Published online: ((will be filled in by the editorial staff))

References

[1] J. W. Yoo, D. J. Irvine, D. E. Discher, S. Mitragotri, Nat. Rev. Drug Discov. 2011, 10, 521; X. J. Wang, J. Feng, Y. C. Bai, Q. Zhang, Y. D. Yin, Chem. Rev. 2016, 116, 10983; R. Mout, D. F. Moyano, S. Rana, V. M. Rotello, Chem. Soc. Rev. 2012, 41, 2539.

[2] A. H. Lu, E. L. Salabas, F. Schuth, Angew. Chem.-Int. Edit. 2007, 46, 1222.

[3] X. H. Yan, Q. Zhou, M. Vincent, Y. Deng, J. F. Yu, J. B. Xu, T. T. Xu, T. Tang, L. M. Bian, Y. X. J. Wang, K. Kostarelos, L. Zhang, Sci. Robot. 2017, 2, 14.

[4] L. S. Xie, X. Pang, X. H. Yan, Q. X. Dai, H. R. Lin, J. Ye, Y. Cheng, Q. L. Zhao, X. Ma, X. Z. Zhang, G. Liu, X. Y. Chen, ACS Nano 2020, 14, 2880.

[5] E. O. Wilson, Science (New York, N.Y.) 1985, 228, 1489; H. C. Berg, D. A. Brown, Nature 1972, 239, 500; A. Gelblum, I. Pinkoviezky, E. Fonio, A. Ghosh, N. Gov, O. Feinerman, Nat. Commun. 2015, 6, 9.

[6] J. Palacci, S. Sacanna, A. P. Steinberg, D. J. Pine, P. M. Chaikin, Science 2013, 339, 936; W. Wang, W. T. Duan, S. Ahmed, A. Sen, T. E. Mallouk, Accounts Chem. Res. 2015, 48, 1938; O. Felfoul, M. Mohammadi, S. Taherkhani, D. de Lanauze, Y. Z. Xu, D. Loghin, S. Essa, S. Jancik, D. Houle, M. Lafleur, L. Gaboury, M. Tabrizian, N. Kaou, M. Atkin, T. Vuong, G. Batist, N. Beauchemin, D. Radzioch, S. Martel, Nat. Nanotechnol. 2016, 11, 941; P. Illien, R. Golestanian, A. Sen, Chem. Soc. Rev. 2017, 46, 5508; M. L. Chen, Z. H. Lin, M. J. Xuan, X. K. Lin, M. C. Yang, L. R. Dai, Q. He, Angew. Chem.-Int. Edit. 2021, 60, 16674; C. R. Chen, X. C. Chang, H. Teymourian, D. E. Ramirez-Herrera, B. Esteban-Fernandez de Avila, X. L. Lu, J. X. Li, S. He, C. C. Fang, Y. Y. Liang, F. Z. Mou, J. G. Guan, J. Wang, Angew. Chem.-Int. Edit. 2018, 57, 241; A. C. Hortelao, C. Simo, M. Guix, S. Guallar-Garrido, E. Julian, D. Vilela, L. Rejc, P. Ramos-Cabrer, U. Cossio, V. Gomez-Vallejo, T. Patino, J. Llop, S. Sanchez, Sci. Robot. 2021, 6, eabd2823; C. J. Wu, J. Dai, X. F. Li, L. Gao, J. Z. Wang, J. Liu, J. Zheng, X. J. Zhan, J. W. Chen, X. Cheng, M. C. Yang, J. Y. Tang, Nat. Nanotechnol. 2021, 16, 288; C. H. Meredith, P. G. Moerman, J. Groenewold, Y. J. Chiu, W. K. Kegel, A. van Blaaderen, L. D. Zarzar, Nat. Chem. 2020, 12, 1136.

[7] M. Vilfan, A. Potocnik, B. Kavcic, N. Osterman, I. Poberaj, A. Vilfan, D. Babic, Proceedings of the National Academy of Sciences of the United States of America 2010, 107, 1844; F. Martinez-Pedrero, P. Tierno, Phys. Rev. Appl. 2015, 3, 051003; H. Xie, M. Sun, X. Fan, Z. Lin, W. Chen, L. Wang, L. Dong, Q. He, Sci. Robot. 2019, 4, eaav8006.

[8] D. Ahmed, T. Baasch, N. Blondel, N. Laubli, J. Dual, B. J. Nelson, Nat. Commun. 2017, 8, 770.

[9] Q. Wang, K. F. Chan, K. Schweizer, X. Du, D. Jin, S. C. H. Yu, B. J. Nelson, L. Zhang, Science advances 2021, 7, eabe5914.

[10] H. Wang, M. Pumera, Chem. Soc. Rev. 2020, 49, 3211.

[11] X. J. Fan, X. G. Dong, A. C. Karacakol, H. Xie, M. Sitti, Proceedings of the National Academy of Sciences of the United States of America 2020, 117, 27916.

[12] J. J. Abbott, K. E. Peyer, M. C. Lagomarsino, L. Zhang, L. X. Dong, I. K. Kaliakatsos, B. J. Nelson, International Journal of Robotics Research 2009, 28, 1434; R. S. M. Rikken, R. J. M. Nolte, J. C. Maan, J. C. M. van Hest, D. A. Wilson, P. C. M. Christianen, Soft Matter 2014, 10, 1295.

[13] J. Yu, D. Jin, K.-F. Chan, Q. Wang, K. Yuan, L. Zhang, Nat. Commun. 2019, 10, 5631.

[14] Q. Wang, D. Jin, B. Wang, N. Xia, H. Ko, B. Y. M. Ip, T. W. H. Leung, S. C. H. Yu, L. Zhang, IEEE/ASME Transactions on Mechatronics 2021, 1.

[15] S. S. Virani, A. Alonso, E. J. Benjamin, M. S. Bittencourt, C. W. Callaway, A. P. Carson, A. M. Chamberlain, A. R. Chang, S. Cheng, F. N. Delling, L. Djousse, M. S. V. Elkind, J. F. Ferguson, M. Fornage, S. S. Khan, B. M. Kissela, K. L. Knutson, T. W. Kwan, D. T. Lackland, T. T. Lewis, J. H. Lichtman, C. T. Longenecker, M. S. Loop, P. L. Lutsey, S. S. Martin, K. Matsushita, A. E. Moran, M. E. Mussolino, A. M. Perak, W. D. Rosamond, G. A. Roth, U. K. A. Sampson, G. M. Satou, E. B. Schroeder, S. H. Shah, C. M. Shay, N. L. Spartano, A. Stokes, D. L. Tirschwell, L. B. VanWagner, C. W. Tsao, C. Amer Heart Assoc, Circulation 2020, 141, E139; G. E. Raskob, P. Angchaisuksiri, A. N. Blanco, H. Buller, A. Gallus, B. J. Hunt, E. M. Hylek, A. Kakkar, S. V. Konstantinides, M. McCumber, Y. Ozaki, A. Wendelboe, J. I. Weitz, I. S. C. World, Arterioscler. Thromb. Vasc. Biol. 2014, 34, 2363.

[16] N. Mackman, Nature 2008, 451, 914.

[17] B. Furie, B. C. Furie, N. Engl. J. Med. 2008, 359, 938; G. Lippi, M. Franchini, G. Targher, Nat. Rev. Cardiol. 2011, 8, 502.

[18] W. J. Powers, A. A. Rabinstein, T. Ackerson, O. M. Adeoye, N. C. Bambakidis, K. Becker, J. Biller, M. Brown, B. M. Demaerschalk, B. Hoh, E. C. Jauch, C. S. Kidwell, T. M. Leslie-Mazwi, B. Ovbiagele, P. A. Scott, K. N. Sheth, A. M. Southerland, D. V. Summers, D. L. Tirschwell, C. Amer Heart Assoc Stroke, Stroke 2019, 50, E344.

[19] E. L. Madison, E. J. Goldsmith, R. D. Gerard, M. J. Gething, J. F. Sambrook, Nature 1989, 339, 721.

[20] S. Vedantham, S. Z. Goldhaber, J. A. Julian, S. R. Kahn, M. R. Jaff, D. J. Cohen, E. Magnuson, M. K. Razavi, A. J. Comerota, H. L. Gornik, T. P. Murphy, L. Lewis, J. R. Duncan, P. Nieters, M. C. Derfler, M. Filion, C. S. Gu, S. Kee, J. Schneider, N. Saad, M. Blinder, S.

Moll, D. Sacks, J. Lin, J. Rundback, M. Garcia, R. Razdan, E. VanderWoude, V. Marques, C. Kearon, A. T. Investigators, N. Engl. J. Med. 2017, 377, 2240; M. W. Mewissen, G. R. Seabrook, M. H. Meissner, J. Cynamon, N. Labropoulos, S. H. Haughton, Radiology 1999, 211, 39.

[21] R. Cheng, W. J. Huang, L. J. Huang, B. Yang, L. D. Mao, K. L. Jin, Q. C. ZhuGe, Y. P. Zhao, ACS Nano 2014, 8, 7746.

[22] J. N. Hu, W. J. Huang, S. W. Huang, Q. C. Zhuge, K. L. Jin, Y. P. Zhao, Nano Res. 2016, 9, 2652.

[23] H. Deng, X. L. Li, Q. Peng, X. Wang, J. P. Chen, Y. D. Li, Angew. Chem.-Int. Edit. 2005, 44, 2782.

[24] J. Xu, Y. Zhang, J. Xu, G. Liu, C. Di, X. Zhao, X. Li, Y. Li, N. Pang, C. Yang, Y. Li, B. Li, Z. Lu, M. Wang, K. Dai, R. Yan, S. Li, G. Nie, Advanced materials (Deerfield Beach, Fla.) 2020, 32, e1905145.

[25] J. Zhou, L. Meng, X. Feng, X. Zhang, Q. Lu, Angewandte Chemie (International ed. in English) 2010, 49, 8476.

[26] T. W. R. Fountain, P. V. Kailat, J. J. Abbott, Ieee, "Wireless Control of Magnetic Helical Microrobots using a Rotating-Permanent-Magnet Manipulator", presented at *IEEE International Conference on Robotics and Automation (ICRA)*, Anchorage, AK, May 03-08, 2010.

[27] D. Walker, B. T. Kasdorf, H. H. Jeong, O. Lieleg, P. Fischer, Science advances 2015, 1, e1500501.

[28] R. Weissleder, D. D. Stark, B. L. Engelstad, B. R. Bacon, C. C. Compton, D. L. White, P. Jacobs, J. Lewis, AJR. American journal of roentgenology 1989, 152, 167.

[29] N. Korin, M. Kanapathipillai, B. D. Matthews, M. Crescente, A. Brill, T. Mammoto, K. Ghosh, S. Jurek, S. A. Bencherif, D. Bhatta, A. U. Coskun, C. L. Feldman, D. D. Wagner, D. E. Ingber, Science 2012, 337, 738.

[30] M. Wan, Q. Wang, R. Wang, R. Wu, T. Li, D. Fang, Y. Huang, Y. Yu, L. Fang, X. Wang, Y. Zhang, Z. Miao, B. Zhao, F. Wang, C. Mao, Q. Jiang, X. Xu, D. Shi, Science advances 2020, 6, eaaz9014.

[31] E. Voros, M. Cho, M. Ramirez, A. L. Palange, E. De Rosa, J. Key, Z. Garami, A. B. Lumsden, P. Decuzzi, Adv. Funct. Mater. 2015, 25, 1709; S. Wang, X. Guo, W. Xiu, Y. Liu, L. Ren, H. Xiao, F. Yang, Y. Gao, C. Xu, L. Wang, Science advances 2020, 6, eaaz8204.

[32] Q. Q. Deng, L. Zhang, W. Lv, X. M. Liu, J. S. Ren, X. G. Qu, ACS Nano 2021, 15, 6604.

[33] M. H. Xie, W. Zhang, C. Y. Fan, C. Wu, Q. S. Feng, J. J. Wu, Y. Z. Li, R. Gao, Z. G. Li, Q. G. Wang, Y. Cheng, B. He, Adv. Mater. 2020, 32, 2000366.

[34] D. Inzitari, M. Eliasziw, P. Gates, B. L. Sharpe, R. K. T. Chan, H. E. Meldrum, H. J. M. Barnett, N. A. S. C. Endar, N. Engl. J. Med. 2000, 342, 1693; M. L. Flaherty, B. Kissela, J. C. Khoury, K. Alwell, C. J. Moomaw, D. Woo, P. Khatri, S. Ferioli, O. Adeoye, J. R. Broderick, D. Kleindorfer, Neuroepidemiology 2013, 40, 36.

[35] R. M. H. McMinn, R. T. Hutchings, J. Pegington, P. Abrahams, *A colour atlas of human anatomy*, Vol. 39, Forensic Science International 1988.

An injectable thrombolytic tool for fast thrombolysis in vivo using low drug dosage is reported, highlighting integrated pharmacomechanical function of synergistic enzyme-magnetite (rtPA-Fe_3O_4) nanoparticle swarms in rabbit carotid artery.

Xiuzhen Tang,[1, 2, 4#] Laliphat Manamanchaiyaporn, [2, 3, 4#] Qi Zhou,[5#] Chenyang Huang,[3] Lihuang Li,[6] Ziqiao Li,[2] Longchen Wang,[1] Jienan Wang,[1] Lei Ren,[6] Tiantian Xu,[3*] Xiaohui Yan,[1, 2*] Yuanyi Zheng[1*]

Synergistic Integration and Pharmacomechanical Function of Enzyme-magnetite Nanoparticle Swarms for Low-dose Fast Thrombolysis